Acta Crystallographica Section A
Foundations of Crystallography
ISSN 0108-7673

Received 3 January 2000
Accepted 8 May 2000

Statistical dynamical direct methods. I. The effective kinematical approximation

J. J. Hu, F. N. Chukhovskii and L. D. Marks*

Northwestern University, Evanston, IL 60208-3108, USA. Correspondence e-mail: l-marks@nwu.edu

While it is known that the kinematical approximation works poorly if at all for transmission electron diffraction, substantial success has been achieved over the last few years in applying it *via* direct methods to determine atomic structures. This raises an interesting quandary; is the established theory of electron diffraction wrong, or are the apparent successes mirages? The intention of this note is to look more deeply into this question and it is found that the correct answer is neither of the above. Beyond vanishingly thin samples when the kinematical approximation holds rigorously, the distribution of phases can remain effectively kinematical; the $\sum_0$ distribution given by the sum of the phase of $+\mathbf{g}$ and $-\mathbf{g}$ reflections remains peaked, albeit not at zero phase, and has a relatively narrow distribution. This fact is shown *via* both exploiting prior works on including anomalous-scattering effects into direct methods, and numerical calculations. Provided that the $\sum_0$ distribution remains narrow, direct methods and indeed structural refinements have some validity. Even larger unit-cell structures with close to statistically random atomic positions do not approach a kinematical limit but instead an effective statistical kinematical approximation. While there are similarities to what there is in conventional (kinematical) direct methods, there remain major differences; for instance, positivity is no longer a valid constraint and the scattering need not be dominated by heavy atoms.

© 2000 International Union of Crystallography
Printed in Great Britain – all rights reserved

1. Introduction

A classic problem in transmission electron diffraction (TED) and microscopy is to determine at least approximately the atomic structure. Over the last 15 years, there has been substantial success in this using high-resolution electron-microscopy (HREM) techniques, coupled as appropriately with image simulations and in some cases powder X-ray diffraction analyses (*e.g.* Spence, 1988; Buseck *et al.*, 1988). Provided that the images are not interpreted too naively, in general they show the atomic structure to a resolution of 0.2 nm or better and approximate atomic positions can be found with a ruler. More challenging is the issue of getting atomic positions to an accuracy of better than 0.05 nm. Quite some time ago, it was shown that a large number of effects, both microscope aberrations as well as dynamical diffraction phenomena (*e.g.* Spence, 1988; Buseck *et al.*, 1988; Cochayne & Gronsky, 1981; Treacey *et al.*, 1985; Saxton & Smith, 1985; Self *et al.*, 1985) could lead to artifacts. Despite these, with due care it is possible to refine atomic positions at defects (*e.g.* see Zhang *et al.*, 1994; Zandbergen *et al.*, 1997; He *et al.*, 1997).

To overcome this problem, one can correct the microscope aberrations, a process that looks like it will work in the near future (Haider, Rose *et al.*, 1998; Haider, Uhlemann *et al.*, 1998). Alternatively, one can avoid any aberrations by dealing directly with the diffraction data where the intensities can be measured to an accuracy of 5% or better using cross-correlation techniques (Xu *et al.*, 1994). Either exploiting some phases obtained from images or just by using these intensities, direct methods appear to be an attractive approach to exploit. Since the region from which diffraction is taken (in a microscope) is small, less than 0.1 μm in routine machines, there are few if any problems with polycrystalline samples. In addition, radiation damage is much less severe with diffraction than in imaging since much lower doses are required. Some substantial successes have been reported using this general approach, either phase extension or full *ab initio* direct methods (Dorset, 1995). Inorganic compounds were first solved using electron diffraction data sets collected from textured structures (Vainshtein, 1964; Vainshtein *et al.*, 1992). More recently, direct methods have been successfully used, for instance, to solve organic crystal structures from electron diffraction data (Dorset, 1996, 1998), zeolites (Nicolopoulos *et al.*, 1998), ceramic oxides (Sinkler *et al.*, 1998), a precipitate Al_mFe in aluminium alloys (Gjønnes *et al.*, 1998) and a new modification of Ti_2Se, the β-phase, and several related inorganic crystal structures (Weirich *et al.*, 2000). Very recently, the prospects and some of the problems in kinematical least-squares

refinement for polymer electron crystallography have been discussed by Dorset & Gilmore (2000). Except for the work of Sinkler *et al.* (1998), all the above used a conventional (*i.e.* kinematical) approach to direct methods. More often than not, dynamical diffraction effects, which always exist and should never be neglected, have been presumed to not matter.

Any application of direct methods or kinematical refinements raises some fundamental problems. There are some simple cases, for instance a surface, where such refinements are legitimate as a good first approximation, but even here correct results require the inclusion of dynamical effects (*e.g.* Jayaram *et al.*, 1993; Marks & Plass, 1995; Collazo-Davila *et al.*, 1998). It is very well established theoretically that even one atom of a heavy element such as gold is a dynamical scatterer, so there are no cases with real samples where the kinematical approximation is rigorously valid. (While exceedingly thin values such as 2 nm are sometimes reported for sample thickness used in matching experimental HREM images, the actual thickness is certainly larger; the discrepancy is often due to neglecting terms such as sample vibration or beam tilt.)

We have an apparent contradiction: either more than 50 years of electron diffraction, and by inference quantum mechanics, is wrong or the direct-methods successes detailed above are mirages. Neither of these two seems to be at all reasonable. The intention of this note is to examine more closely these issues. We will show that a more subtle analysis of the statistics of the breakdown of the formal kinematical approximation yields some important results that resolve in part the contradiction. Of particular importance is the Σ_0 two-phase structure invariant:

$$\psi(\mathbf{g}) = \varphi(\mathbf{g}) + \varphi(-\mathbf{g}), \tag{1}$$

where $\varphi(\mathbf{g})$ is the phase of the structure factor for the reciprocal-lattice vector $\mathbf{g}$. While this is rigorously equal to $2\pi n$ ($n = 0, \pm 1$) for kinematical diffraction, it is not for dynamical diffraction. However, if in a statistical sense the distribution of Σ_0 values (for different $\mathbf{g}$) has a central peak and a relatively narrow width, the statistics underlying direct methods will remain reasonably valid. The conditions that the distribution is relatively narrow, what we will refer to as an 'effectively kinematical' case, hold to quite respectable thickness. This follows both analytically by combining prior work on anomalous scattering (Hauptman, 1982) coupled with a simple channeling model, and is also confirmed by numerical simulations. Note that, while this implies some similarities to conventional (kinematical) direct methods, there are still major differences. The next stage in developing an understanding of how direct methods can be applied to dynamical diffraction data, *i.e.* the triplet structure invariants, will be discussed elsewhere (Chukhovskii *et al.*, 2000).

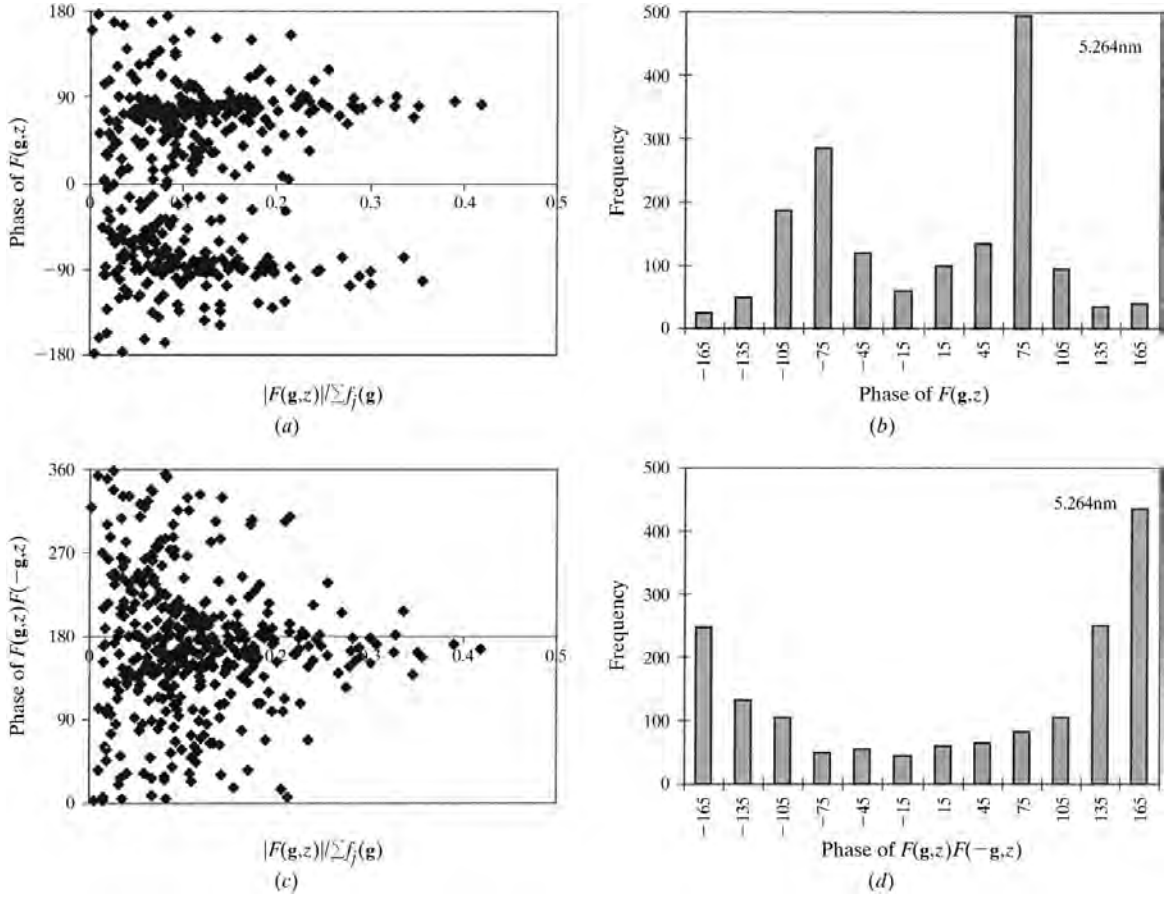

Figure 1
The probability distributions and histograms of the phases of the dynamic structure factors $F(\mathbf{g}, z)$ and the product $F(\mathbf{g}, z)F(-\mathbf{g}, z)$. The crystal thickness z along the [001] zone axis of $C_{32}Br_{16}CuN_8$ is 5.264 nm.

2. Analysis

The general problem of three-dimensional transmission electron diffraction data (*i.e.* that collected from a number of different zone axes) is very difficult; for instance, it is not clear whether it is valid to merge data from different orientations (and with different sample thicknesses). We will limit our analysis to a two-dimensional data set. We will first show by combining a channeling (tight-binding Bloch-wave) model with prior work on anomalous scattering that the Σ_0 distribution will tend to show a peak and relatively narrow width beyond the limit of kinematical diffraction.

It is appropriate to give a short introduction to the tight-binding Bloch-wave model that will be used here. The two standard techniques for calculating dynamical electron diffraction are multislice and Bloch-wave methods, both using plane-wave expansions of the wavefunction. For low-resolution imaging, orientations are generally used (*e.g.* two-beam or systematic row) where the calculations converge with only a few plane-wave terms. However, for a zone-axis orientation, a large number is required, typically out to 40 nm^{-1}. This makes it difficult to generate physical insight into what is going on. An alternative Bloch-wave expansion was first proposed for the case of electron or ion channeling (Berry & Mount, 1972; Kambe *et al.*, 1974), namely to use two-dimensional atomic orbitals, in essence a tight-binding expansion. This expansion has been revived recently after it was pointed out by Van Dyck & Op de Beeck (1996) that for a relatively thin sample only a limited number of atomic orbitals is required to accurately describe the wavefunction if the atomic strings do not overlap appreciably in projection. With a truncated series of two-dimensional orbitals, one can add orthogonalized plane waves [OPWs – see for instance Kittel (1963) or other solid-state physics texts and Appendix *A*] to form a complete basis set. The OPWs interact with the much smaller pseudopotential rather than the full crystal potential, so scattering of the OPW states is weak for a thin crystal. In most cases, only the lowest transverse energy 1*s* states (Bloch-wave state levels) need to be included, and the pseudopotential can be taken as vanishingly weak.

The tight-binding Bloch-wave approximation provides a compact and rather rigorous (exact if all terms in the expansion are used) Bloch-wave expansion for dynamical diffraction effects near a zone-axis orientation, comparable in many ways to the classic two-beam approximation used for low-resolution defect analysis imaging. (The OPW states cannot be neglected

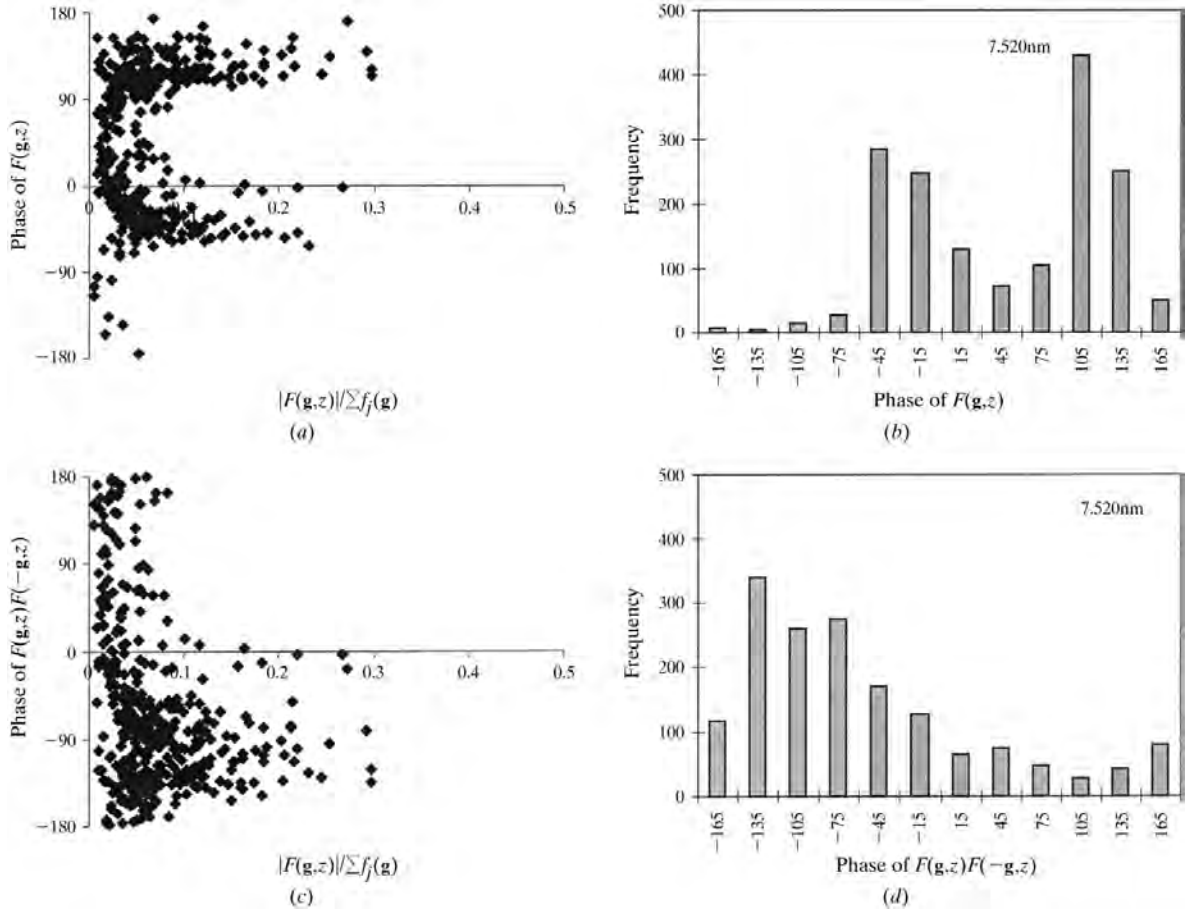

Figure 2
The probability distributions and histograms of the phases of the dynamic structure factors $F(\mathbf{g}, z)$ and the product $F(\mathbf{g}, z)F(-\mathbf{g}, z)$. The crystal thickness z along the [001] zone axis of $C_{32}Br_{16}CuN_8$ is 7.520 nm.

off a zone-axis.) For instance, it has been used to give exact expressions for high-resolution image contrast including dynamical effects (Sinkler & Marks, 1999*a*; Hu & Tanaka 1999) and an approximate method for handling an initial refinement of zone-axis diffraction data (Van Dyck & Chen, 1999). More important, here it shows how atom-like features arise in the real-space wavefunction, and can therefore be used to understand how direct methods work with transmission electron diffraction data, for instance the clarity of light atoms (not just heavy atoms) in many materials (Sinkler & Marks, 1999*b*).

As discussed in more detail in Appendix *A*, we can write a complete solution for the electron wavefunction in a thin crystal as a sum over two-dimensional channeling eigenstates $\Psi_n(\mathbf{R}, z)$, where $\mathbf{R} = (x, y)$ is a two-dimensional vector perpendicular to the electron-beam direction, namely:

$$\Psi(\mathbf{R}, z) = 1 + \sum_n a_n \Psi_n(\mathbf{R})\{\exp[-i\pi(E_n/E_0)\kappa z] - 1\}. \quad (2)$$

The sum in equation (2) is over the eigenstates labeled n, with occupations a_n. Each eigenstate has a characteristic oscillation frequency as a function of depth z, which is determined by the channeling (Bloch-wave) eigenvalue E_n (E_0 being the incident electron energy and $\kappa = \lambda^{-1}$). For a thin crystal, this series solution can be legitimately truncated after including only the most significant terms (see Appendix *A*). For moderate values of sample thickness and atomic numbers, a further simplification of (2) can be used for cases in which the atomic columns are well separated in projection so that the atomic potentials do not strongly overlap (Van Dyck & Op de Beeck, 1996). (Note that, in a standard perturbation expansion, rehybridization effects will scale with the degree of overlap.) In such cases, the lowest-lying eigenstate E_j (analogous to the j atomic 1*s* state) mainly contributes to the sum on the right-hand side of (2), so the electron wavefunction may be written as

$$\Psi(\mathbf{R}, z) = 1 - 2i \sum_j a_j \Psi_j(\mathbf{R} - \mathbf{R}_j) \exp[-i\pi(E_j/2E_0)\kappa z] \times \sin[\pi(E_j/2E_0)\kappa z], \quad (3)$$

where now the sum is over the j atomic positions.

We will now use this form and do a relatively standard direct-methods analysis for the $\sum_0$ conditional probability distribution. Switching to reciprocal space, the standard space used in structure analyses, the normalized structure factor for the **g** reflection takes the form

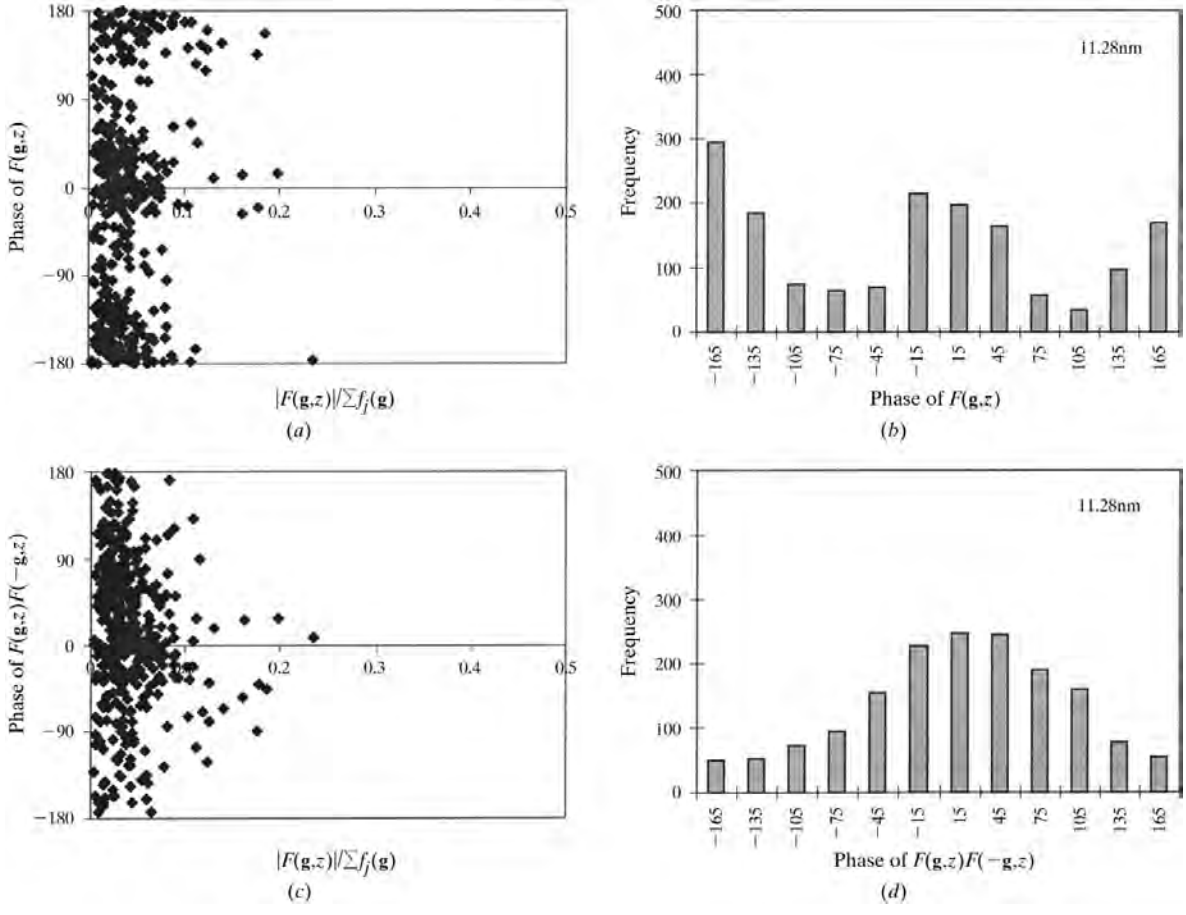

Figure 3
The probability distributions and histograms of the phases of the dynamic structure factors $F(\mathbf{g}, z)$ and the product $F(\mathbf{g}, z)F(-\mathbf{g}, z)$. The crystal thickness z along the [001] zone axis of $C_{32}Br_{16}CuN_8$ is 11.28 nm.

$$U_{\mathbf{g}} \equiv F_{\mathbf{g}}/\varepsilon_{\mathbf{g}}^{1/2} = \varepsilon_{\mathbf{g}}^{-1/2} \sum_{j=1}^{N} |F_{j\mathbf{g}}| \exp[i(\delta_{j\mathbf{g}} - 2\pi \mathbf{g}\cdot\mathbf{r}_j)], \quad (4)$$

where

$$F_{j\mathbf{g}} = |F_{j\mathbf{g}}| \exp(i\delta_{j\mathbf{g}}) \quad (5)$$

$$= 2V_j(\mathbf{g}) \exp[-i\pi/2 - i\pi(E_j/2E_0)\kappa z] \sin[\pi(E_j/2E_0)\kappa z] \quad (6)$$

is the complex atomic scattering amplitude of the atom labeled j, $\mathbf{r}_j$ its position vector and N the number of atoms in the unit cell. The normalization factor $\varepsilon_{\mathbf{g}}$ is equal to

$$\varepsilon_{\mathbf{g}} = \sum_{j=1}^{N} |F_{j\mathbf{g}}|^2 \quad (7)$$

with $V_j(\mathbf{g})$ the Fourier transform of $\Psi_j(\mathbf{R} - \mathbf{R}_j)$, to a first approximation the kinematical single-atom structure factor. In the limit of a vanishingly small thickness, one has then $\psi(\mathbf{g}) = 0 \quad [\varphi(-\mathbf{g}) = -\varphi(\mathbf{g})]$. The conditional probability distribution (CPD) $P(\psi(\mathbf{g})|R_{\mathbf{g}}, R_{-\mathbf{g}})$ defined for the value of $\psi(\mathbf{g})$ and the two magnitudes $R_{\mathbf{g}} = |U_{\mathbf{g}}|$, $R_{-\mathbf{g}} = |U_{-\mathbf{g}}|$ may be written as (Hauptman, 1982)

$$P(\psi(\mathbf{g})|R_{\mathbf{g}}, R_{-\mathbf{g}}) = \left[2\pi I_0\left(\frac{2R_{\mathbf{g}}R_{-\mathbf{g}}}{1-X^2}\right)\right]^{-1} \times \exp\left\{\left(\frac{2R_{\mathbf{g}}R_{-\mathbf{g}}X}{1-X^2}\right)\cos[\psi(\mathbf{g}) + \xi(\mathbf{g})]\right\}. \quad (8)$$

Here the $\sum_0$ CPD parameters X and ξ are given by

$$X_{\mathbf{g}} \exp(-i\xi_{\mathbf{g}}) = \varepsilon_{\mathbf{g}}^{-1} \sum_{j=1}^{N} |F_{j\mathbf{g}}|^2 \exp(2i\delta_{j\mathbf{g}}), \quad (9)$$

where I_0 is the modified Bessel function. It follows from equation (8) that the $\sum_0$ CPD has a single maximum at $\psi_{\mathbf{g}} = -\xi_{\mathbf{g}}$ (the $\sum_0$ invariant), and the two-phase structure variable is distributed around the value of $-\xi_{\mathbf{g}}$ with a width $\Delta\psi \approx A_{\mathbf{g}}^{-1/2}$. The latter is relatively narrow if the variance of the $\sum_0$ CPD is small, which is inversely proportional to

$$A_{\mathbf{g}} = R_{\mathbf{g}}R_{-\mathbf{g}}X_{\mathbf{g}}/(1 - X_{\mathbf{g}}^2). \quad (10)$$

Going back to (5) and staying in the frame of 1s-state channeling, one finds that the phase of the complex atomic scattering amplitude δ_j does not depend on the diffraction vector $\mathbf{g}$, only on the thickness variable z. Hence, the subscript $\mathbf{g}$ can be omitted in the symbols $\delta_{j\mathbf{g}}$, $X_{\mathbf{g}}$ and $\xi_{\mathbf{g}}$, and the $\sum_0$ invariant

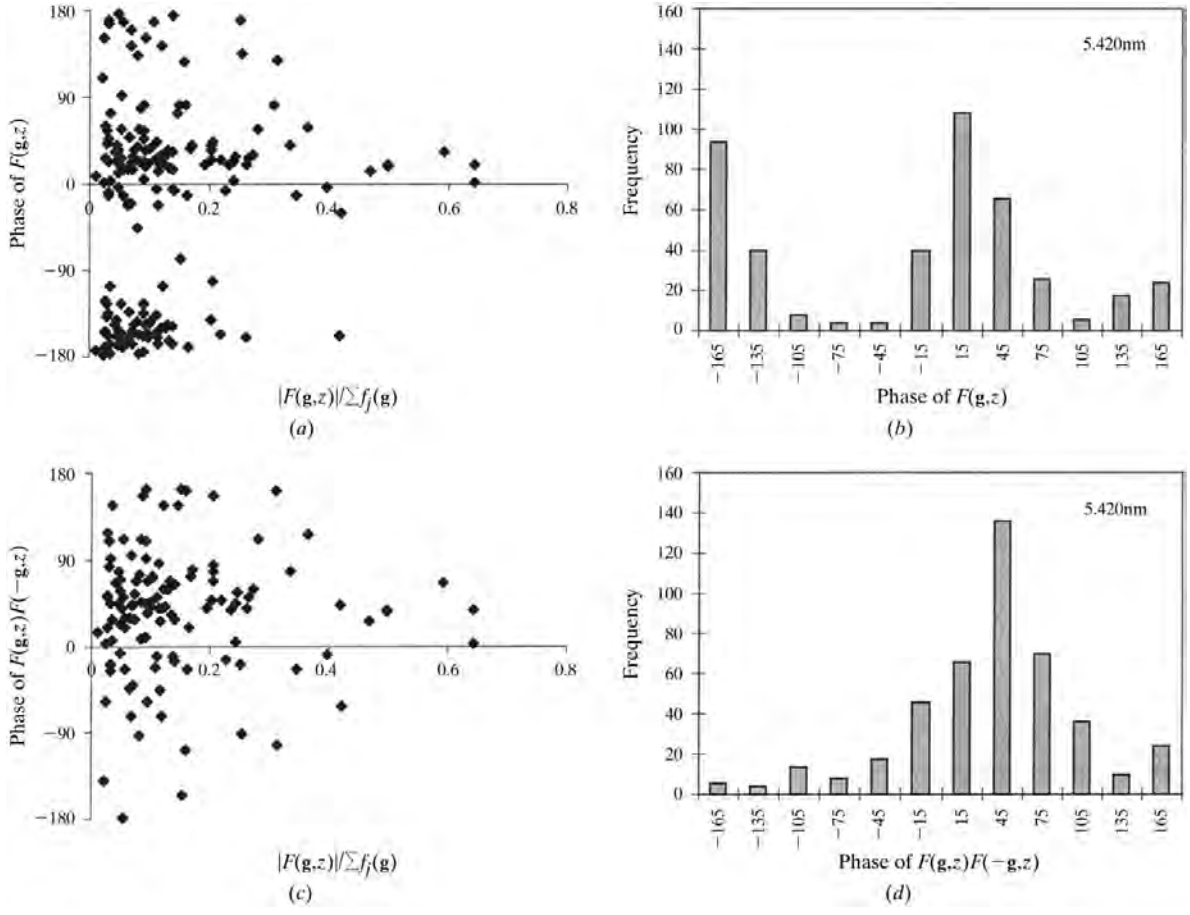

Figure 4
The probability distributions and histograms of the phases of the dynamic structure factor $F(\mathbf{g}, z)$ and the product $F(\mathbf{g}, z)F(-\mathbf{g}, z)$. The crystal thickness z along the [001] zone axis of $YSr_2Cu_2GaO_7$ is 5.42 nm.

(equal to $-\xi$) has a unique value that does not depend on the diffraction vector **g**.

To condense this into very simple mathematical terms, the true wavefunction $\Psi(\mathbf{r}, z)$ can be relatively well approximated *in a statistical sense* as

$$\Psi(\mathbf{r}, z) \approx 1 + \Phi(\mathbf{r}, z) \exp[i\varphi(z)], \tag{11}$$

where $\Phi(\mathbf{r}, z)$ is a real function which we call the effective potential, and the approximation is better obeyed for the stronger reflections in reciprocal space. Note that, while it follows directly from the tight-binding analysis that $\Phi(\mathbf{r}, z)$ has atomistic character, there is no guarantee that it is positive or dominated by heavier atoms. Some of the statistical characteristics that are normally associated with kinematical scattering still apply, even though in a numerical sense the kinematical approximate is not even close to valid.

3. Numerical simulations. Results

The connection detailed above between a 1*s*-state channeling model and the $\sum_0$ CPD derived using the same arguments that have been applied for anomalous-scattering effects in X-ray diffraction needs to be tested against proper dynamical diffraction calculations before any conclusions can be reached. In this section, multislice results are presented for a number of different structures which show that the analytical conclusions in §2 hold well in general for relatively thin samples.

3.1. Copper perbromophthalocyanine $C_{32}Br_{16}CuN_8$

The first test case we will consider is copper perbromophthalocyanine ($C_{32}Br_{16}CuN_8$) (Dorset *et al.*, 1992). The slice thickness along the beam incident direction was $c = 0.376$ nm, the projected two-dimensional axes were $a = 1.756$ and $b = 2.608$ nm, and calculations were performed for an accelerating voltage of 200 kV. It is a centrosymmetric structure with space group $C2/c$. Figs. 1(*a*) and 1(*c*) show the numerically simulated one- and two-phase probability distributions for the dynamic single $F(\mathbf{g}, z)$ and the product of $F(\mathbf{g}, z)F(-\mathbf{g}, z)$ structure factors, respectively. The phase is plotted *versus* the corresponding amplitude that was normalized by using single atomic scattering coefficients within a unit cell in order to show the values on a unitary scale, and the 0 beam was normalized as 1. The corresponding histograms of the frequency of phases are given in Figs. 1(*b*) and 1(*d*). The crystal thickness used in Fig. 1 is $z = 5.264$ nm. Figs. 2 and 3 show the same behavior for thicknesses of $z = 7.520$ and

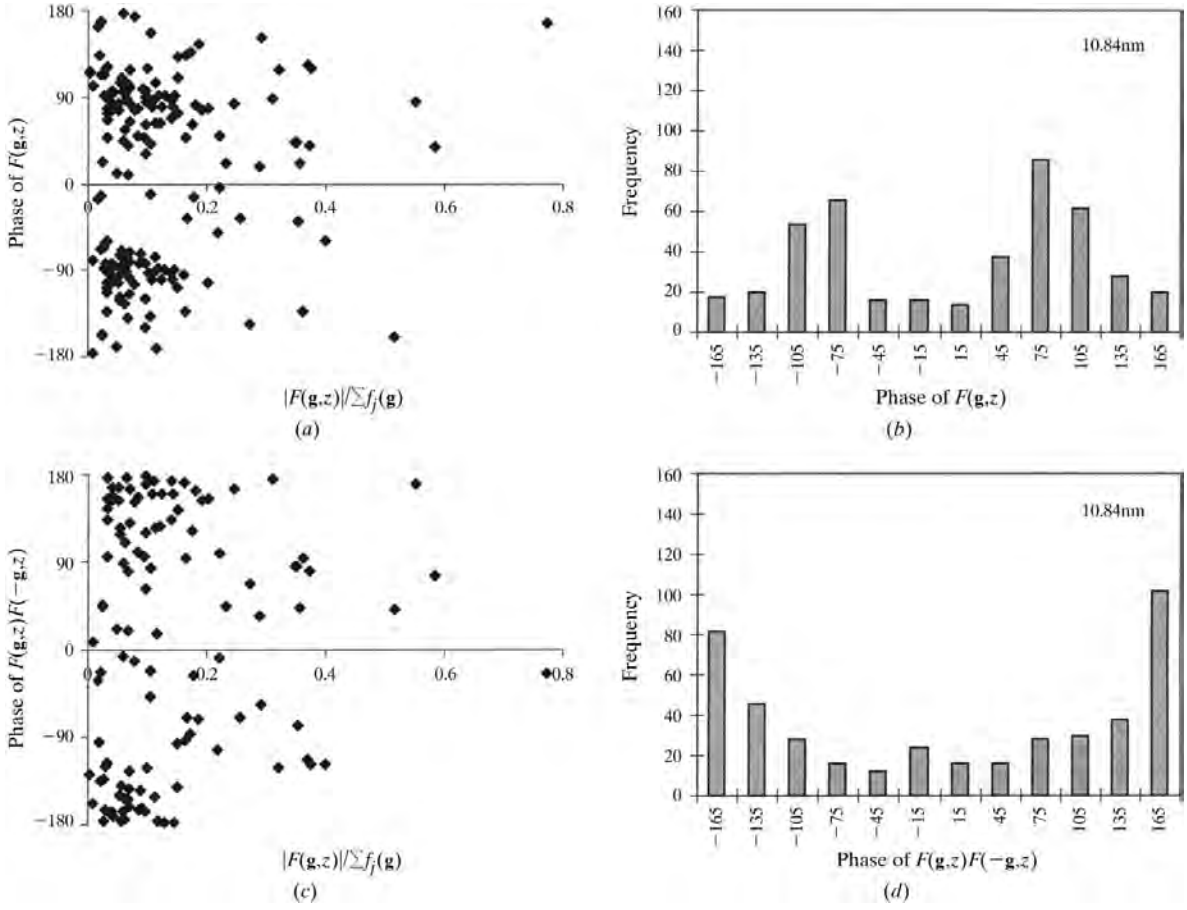

Figure 5
The probability distributions and histograms of the phases of the dynamic structure factor $F(\mathbf{g}, z)$ and the product $F(\mathbf{g}, z)F(-\mathbf{g}, z)$. The crystal thickness z along the [001] zone axis of $YSr_2Cu_2GaO_7$ is 10.84 nm.

$z = 11.28$ nm, respectively. It can be seen from these figures that the phase distribution of the dynamical $F(\mathbf{g}, z)$ has two peaks separated by about 180°, and that the phases of the product, $\sum_0$, tends to a constant value. Within a range of 30°, the maximum is 20–30% of a total of 1629 diffraction beams within a circle of radius 15.0 nm^{-1}. The peak height reduces with increasing crystal thickness, as other states (*e.g.* 2*s*) become more important. It should be noted that the $\sum_0$ CPD has a smaller deviation for larger amplitudes as predicted in §2. (Since there were fewer large amplitudes as the thickness increased, the calculated distribution of phases does not show such a pronounced peak in Fig. 3.)

3.2. Ca-doped $YSr_2Cu_2GaO_7$

The second test structure was the superconducting ceramic of $YSr_2Cu_2GaO_7$, with lattice parameters of $a = 2.2696$, $b = c = 0.542$ nm and $\alpha = \beta = \gamma = 90°$ (Vaughey *et al.*, 1991). As observed previously (Sinkler & Marks, 1999*a*,*b*), a 1*s* channeling model does not describe this material particularly well. Figs. 4 and 5 are the simulated phase distributions at sample thicknesses of 5.42 and 10.84 nm, respectively, again at 200 kV. The number of beams inside a circle of radius 15.0 nm^{-1} was 439. Although the distributions are somewhat wider than those of Figs. 1–3, there is still a tendency for the stronger beams to obey the $\sum_0$ relationship. In particular, the frequency histogram of phases shows a maximum as shown in Figs. 4(*b*), 4(*d*) and 5(*b*), 5(*d*).

3.3. Chlorinated copper phthalocyanine $C_{32}Cl_{16}CuN_8$: centrosymmetric and broken centrosymmetric cases

The last sample used is an artificial structure constructed by switching about half of the atoms in chlorinated copper phthalocyanine ($C_{32}Cl_{16}CuN_8$) to create a broken centrosymmetric structure. It has the same lattice parameters as $C_{32}Br_{16}CuN_8$ (Uyeda *et al.*, 1978–1979). The multislice-calculated results for both the centro- and broken centrosymmetric structures ('random' model) of $C_{32}Cl_{16}CuN_8$, respectively, are shown on the left and right in Figs. 6, 7 and 8; for reference, Table 1 lists the atomic positions used for the random model. We note that for the 'random' model the phase distribution of $F(\mathbf{g}, z)$ does not exhibit any frequency peak (*e.g.* Fig. 6*d*). It is apparent that the 'random' model obeys very well the $\sum_0$ distribution (see Figs. 7*d* and 8*d*). To understand this, it is important to note the connection between what is called in the

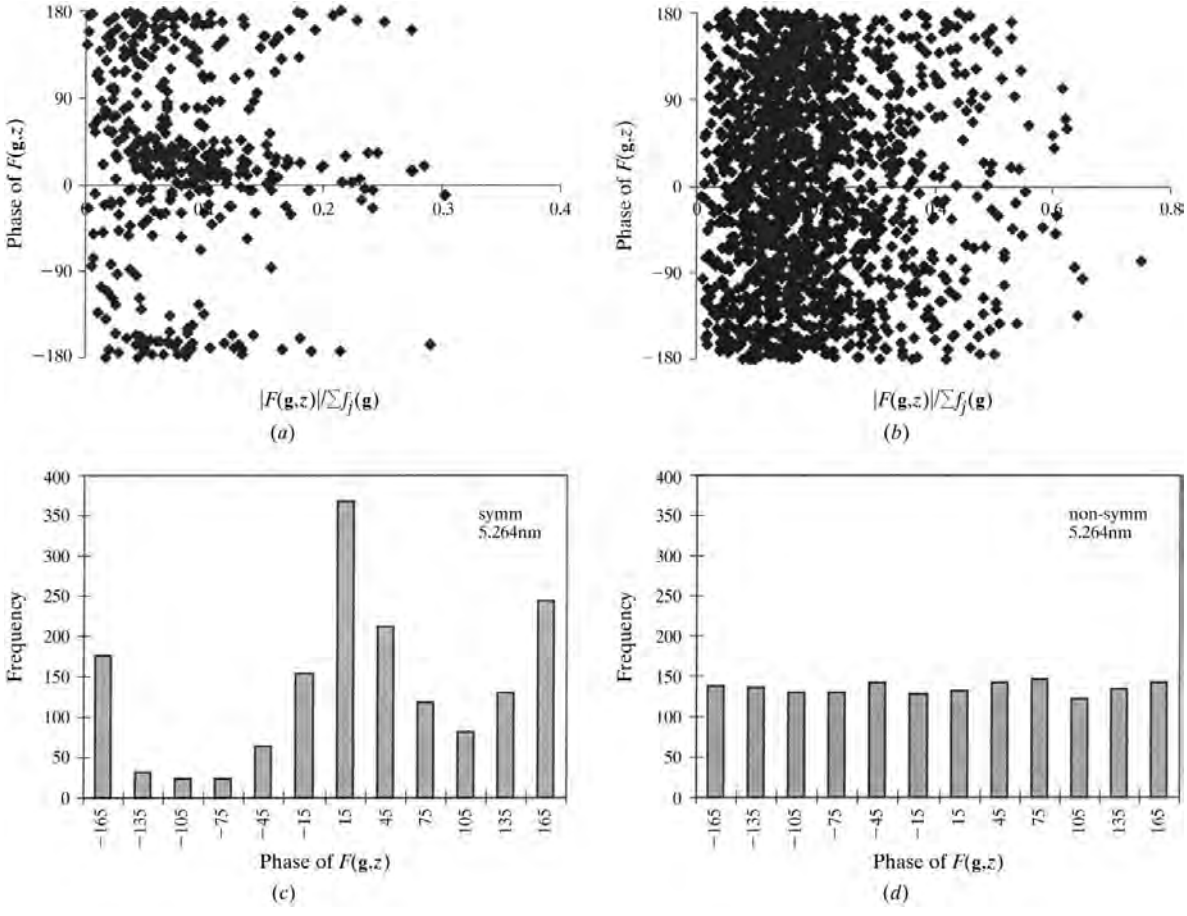

Figure 6
Phase distributions and histograms of the dynamic structure factors $F(\mathbf{g}, z)$ for the centrosymmetric and noncentrosymmetric (random) models of $C_{32}Cl_{16}CuN_8$ crystal.

Table 1
Atomic positions of the broken centrosymmetric structure ('random' model) of $C_{32}Cl_{16}CuN_8$.

	x	*y*	*z*
Cl1	0.919	0.302	0.000
Cl2	0.919	0.698	0.000
Cl3	0.419	0.802	0.000
Cl4	0.419	0.198	0.000
Cl5	0.157	0.202	0.000
Cl6	0.657	0.702	0.000
Cl7	0.843	0.202	0.000
Cl8	0.343	0.702	0.000
Cl9	0.271	0.120	0.000
Cl10	0.771	0.620	0.000
Cl11	0.729	0.120	0.000
Cl12	0.229	0.620	0.000
Cl13	0.595	0.057	0.000
Cl14	0.595	0.943	0.000
Cl15	0.095	0.557	0.000
Cl16	0.095	0.443	0.000
N1	0.000	0.070	0.000
N2	0.500	0.570	0.000
N3	0.093	0.000	0.000
N4	0.593	0.500	0.000
N5	0.883	0.090	0.000
N6	0.883	0.910	0.000
N7	0.383	0.590	0.000
N8	0.383	0.410	0.000

direct-methods literature 'pseudosymmetry' and dynamical diffraction effects. For a 'random' distribution of atomic columns, cross terms will statistically tend to cancel out, similar to an amorphous material (Marks, 1988). When additional pseudosymmetry is present within the unit cell, this may not be the case. It follows that larger-cell materials with more random atomic columns will tend to follow the effective kinematical approximation rather better with a narrow $\sum_0$ distribution. Note that the maximum of the $\sum_0$ distribution is not at 0° (as it is for kinematical diffraction) but shifted.

3.4. Accelerating voltage effect

In addition to sample thickness, accelerating voltage is an independently adjustable parameter. Fig. 9 shows simulated results for $C_{32}Cl_{16}CuN_8$ at voltages of 100 kV, 500 kV and 1 MV, respectively, for a thickness of 5.264 nm. On the left is shown the probability distribution of $\sum_0$ phases *versus* the diffraction amplitude, on the right the corresponding frequency histogram of the phases. Neither the distributions nor the frequency histograms are improved at higher voltage; indeed, as evident in Figs. 9(*c*) and 9(*f*), at 1 MV the results are somewhat worse. The reason for this is

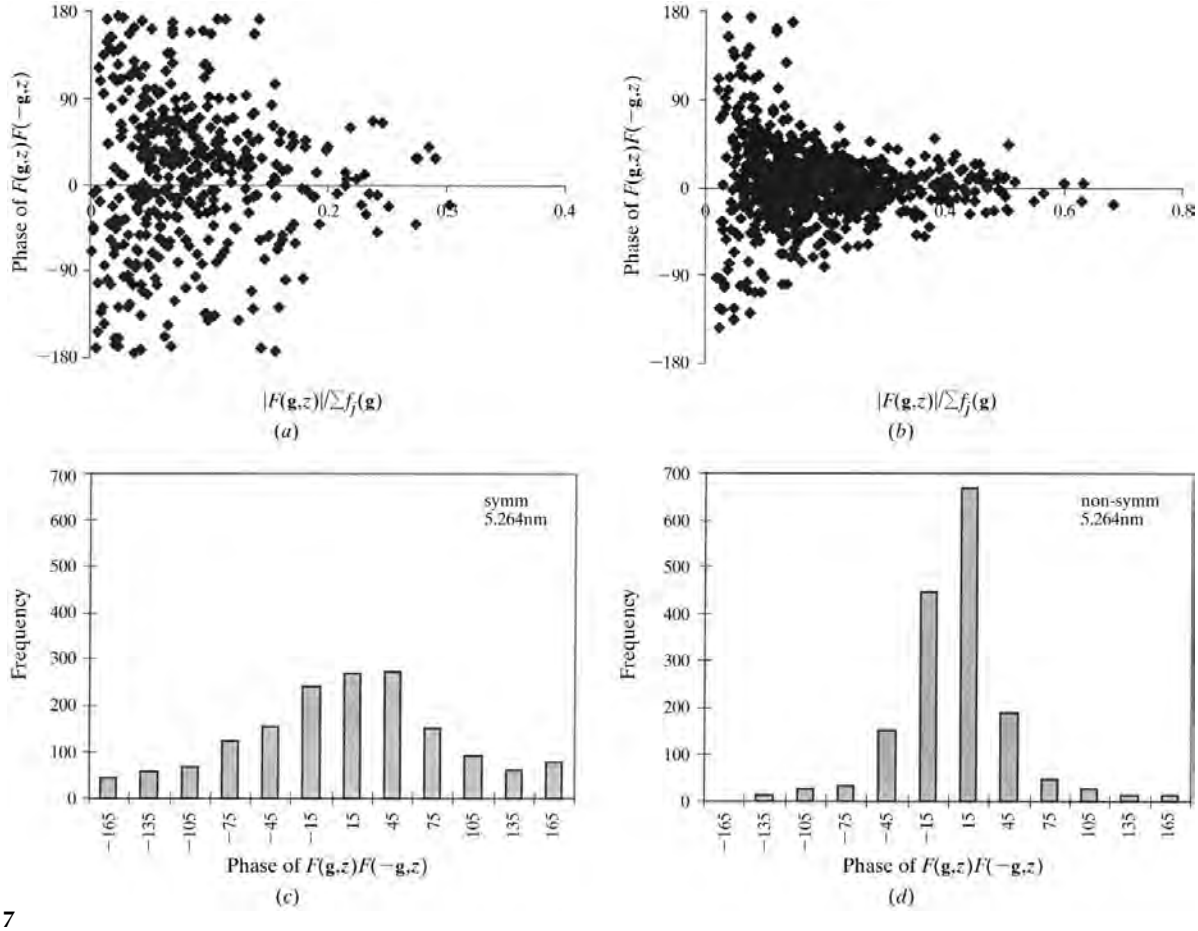

Figure 7
Phase distributions and histograms of the products $F(\mathbf{g}, z)F(-\mathbf{g}, z)$ for the centrosymmetric and noncentrosymmetric (random) models of $C_{32}Cl_{16}CuN_8$ crystal. The sample thickness z along the zone [001] axis is 5.264 nm.

that at higher voltages there are more strongly bound states (*e.g.* 2*s*, 3*s*), which complicate the dynamical diffraction. This is a classic example of the role of relativity in electron diffraction, in that diffraction does not tend towards simple kinematical at higher voltages owing to the increase of the electron effective mass.

4. Discussion

The numerical results presented in the previous section confirm the distribution analysis of §2. While it is certainly not true or even close to true to state that the diffraction is kinematical, in a statistical sense the $\sum_0$ CPD is relatively narrow for some realistic sample thickness. To reiterate what was derived previously, the true wavefunction $\Psi(\mathbf{r}, z)$ can be relatively well approximated *in a statistical sense* as

$$\Psi(\mathbf{r}, z) \approx 1 + \Phi(\mathbf{r}, z)\exp[i\varphi(z)],$$

where $\Phi(\mathbf{r}, z)$ is a real function, which we call the effective potential, and the approximation is better obeyed for the stronger reflections in reciprocal space. Conventional direct methods applied to the diffraction data will tend to recover this effective potential. Note that there is no reason to assume that $\Phi(\mathbf{r}, z)$ is positive and, while it will have maxima or minima at the positions of atomic columns, there is no *a priori* reason to presume any direct scaling between the crystal potential and the effective potential. In certain cases as shown by Sinkler & Marks (1999*b*), light atoms dominate the effective potential. While there are similarities to what one has in conventional (kinematical) direct methods, there are also major differences.

The apparent contradiction that was described in the *Introduction* can now be considered partially resolved. Taken literally, the kinematical approximation is awful for transmission electron diffraction. However, taken statistically, it is reasonable. Furthermore, provided that the effective potential has peaks at the atom sites, which it has for 1*s* channeling, 'refinement' of atomic positions should have some validity. It is worth repeating the point made earlier that larger unit-cell structures with close to statistically random atomic positions do not approach a kinematical limit but instead the effective kinematical approximation. While the existence of this statistical limit rationalizes prior successes using conventional direct methods, this should not be taken as implying that a kinematical approximation is the best way to solve structures

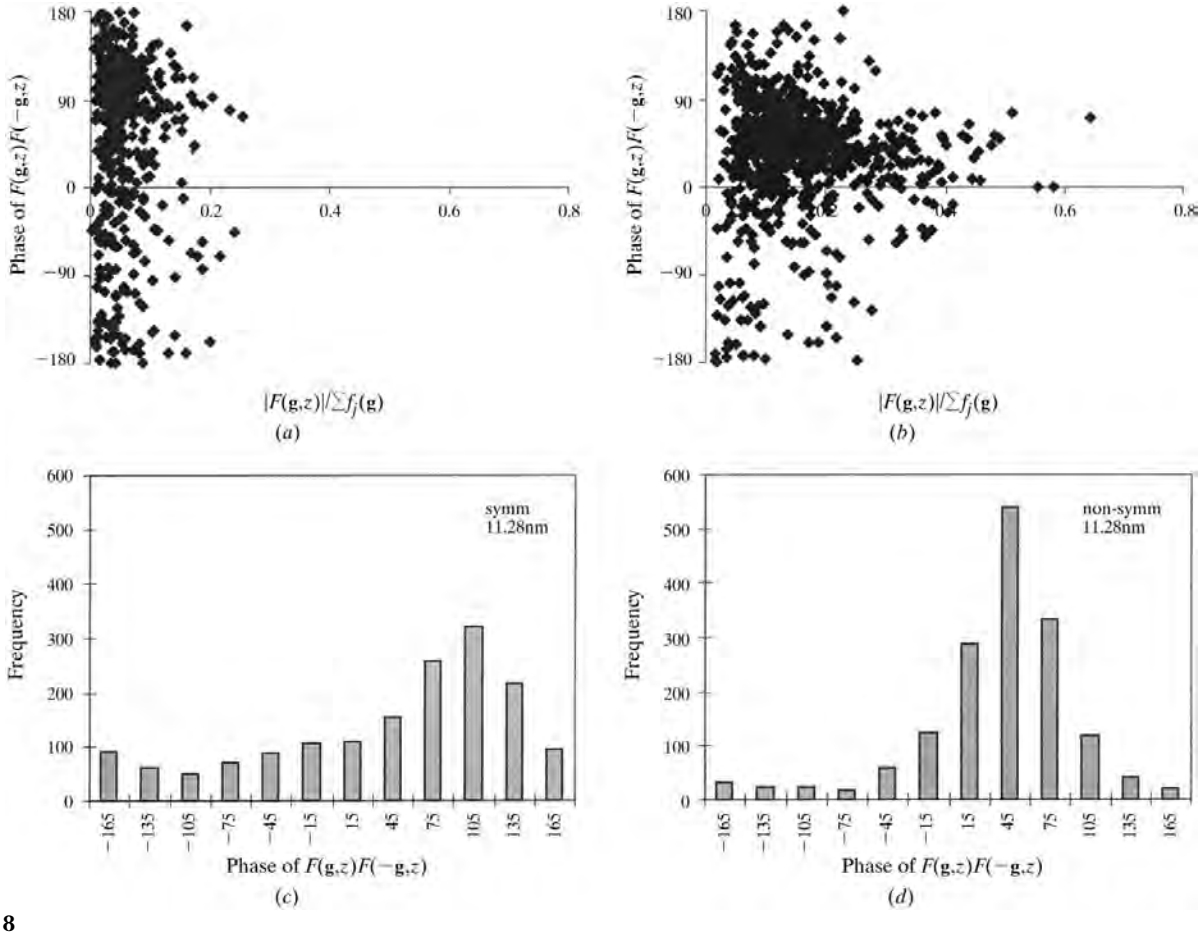

Figure 8
Phase distributions and histograms of the products $F(\mathbf{g}, z)F(-\mathbf{g}, z)$ for the centrosymmetric and noncentrosymmetric (random) models of $C_{32}Cl_{16}CuN_8$ crystal. The sample thickness z along the zone [001] axis is 11.28 nm.

from transmission electron diffraction data; we believe it is not. The more general dynamical triplet case with inclusion of dynamical effects, *i.e.* direct methods with complex terms in real space, will be discussed elsewhere (Chukhovskii *et al.*, 2000).

As a final caveat, it needs to be remembered that the effective kinematical approximation holds well only if the diffraction is dominated by 1*s* states. This is not generally true, and there are many structures where 2*p* states (or, depending how one performs the expansion, the orthogonalized Bloch-wave states) are important, and there can readily be stronger excitation of these if the sample is tilted off the zone axis. The question of whether classical direct methods have any validity in these cases or should be abandoned in favor of approaches that include dynamical effects from the start remains unanswered.

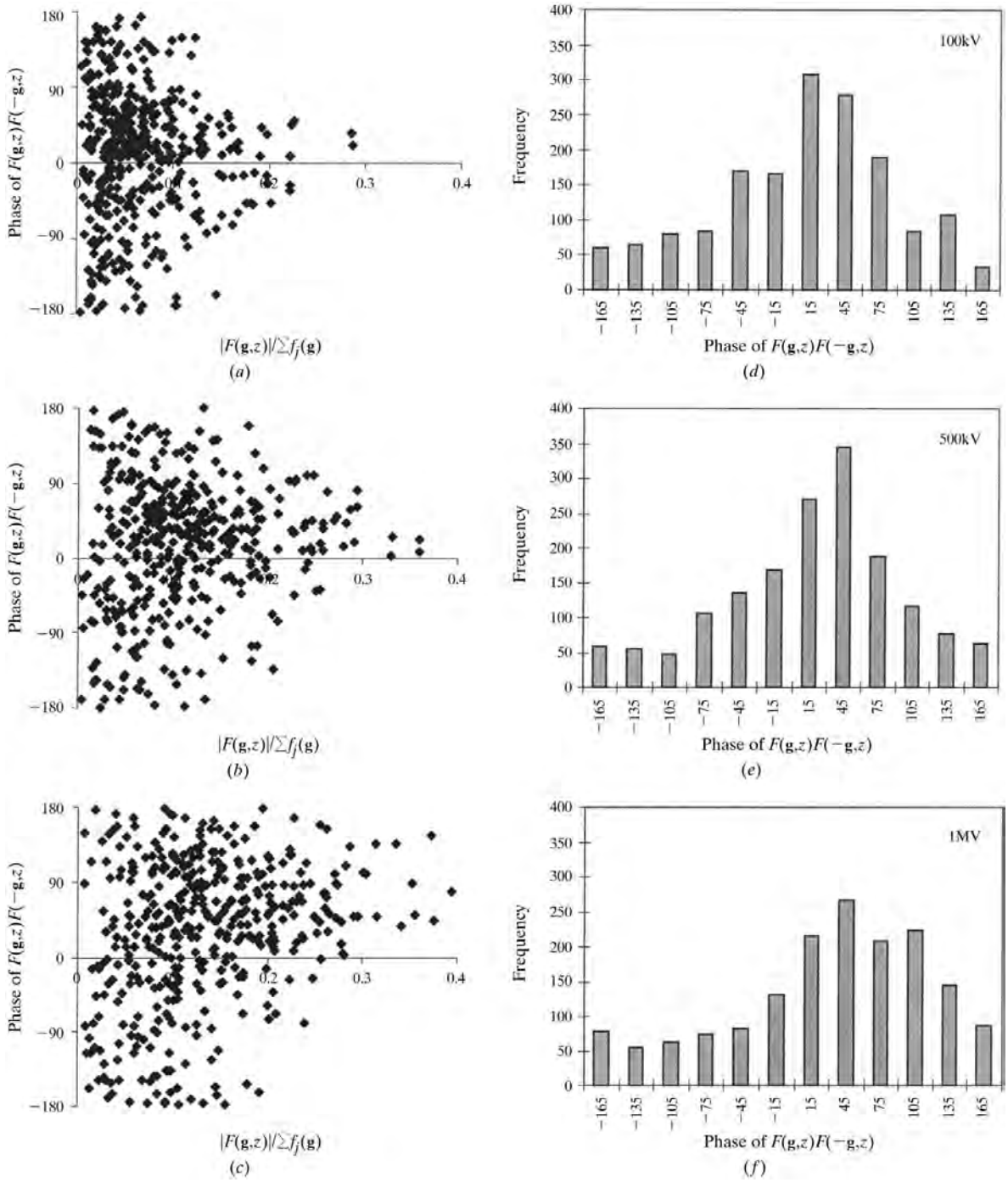

Figure 9
Phase distributions and histograms of $C_{32}Cl_{16}CuN_8$ crystal for different values of accelerating voltage: (*a*), (*d*) 100 kV; (*b*), (*e*) 500 kV; (*c*), (*f*) 1 MV. The sample thickness z along the zone [001] axis is 5.264 nm.

APPENDIX *A*

We will give here a slightly more complete derivation than that of Van Dyck & Op de Beeck (1996). Considering Schrödinger's equation in the high-energy approximation, we look for solutions to the quasi-two-dimensional equation:

$$i\partial/\partial z[\Psi(\mathbf{R}, z)] = H_{\mathbf{R}}\Psi(\mathbf{R}, z), \tag{12}$$

where the two-dimensional Hamiltonian

$$H_{\mathbf{R}} = (1/4\pi k)[-\Delta_{\mathbf{R}} + V(\mathbf{R})], \quad V(\mathbf{R}) = -(8\pi^2 me/h^2)\Pi(\mathbf{R}) \tag{13}$$

and $\Pi(\mathbf{R})$ is the electrostatic crystal potential function averaged along the direction (z axis) of the incoming electron beam, m and k are the relativistic electron mass and inverse wavelength and h is Planck's constant.

We look for a solution $\Psi(\mathbf{R}, z)$ expanded as a series of eigenfunctions for the Hamiltonian (13) in the form

$$\Psi(\mathbf{R}, z) = \sum_c \langle\Psi_c|0\rangle\Psi_c(\mathbf{R})\exp(-i\zeta_c z) + \sum_n C_n(z)\varphi_n(\mathbf{R}). \tag{14}$$

Here we have introduced so-called 'core' eigenfunctions $\Psi_c(\mathbf{R})\exp(-i\zeta_c z)$ and, to complete the solution, orthogonalized plane-wave functions (OPW's) $\varphi_n(\mathbf{R})$ of form

$$\varphi_n(\mathbf{R}) = |n\rangle - \sum_c \langle\Psi_c|n\rangle\Psi_c(\mathbf{R}) \tag{15}$$

[the concise notation $|n\rangle$ implies the plane-wave function $|\mathbf{g}_n\rangle = \exp(i\mathbf{g}_n\cdot\mathbf{R})$, $\mathbf{g}_1 \equiv 0$]. In general, the core eigenfunctions are the lowest lying Wannier functions which we will later approximate as linear combinations of the isolated column two-dimensional orbitals. While one can include all the core states in the expansion, *i.e.* use a conventional Bloch-wave analysis, we choose instead to truncate the series. We will show that such a truncation is legitimate for a thin crystal.

Substituting the wavefunction (14) into Schrödinger's equation (12) yields the following system of equations for the coefficients C_n:

$$i\sum_n \partial/\partial z(C_n)\left\{|n\rangle - \sum_c\langle\Psi_c|n\rangle\Psi_c\right\} = \sum_n C_n\left\{[\xi_n + \mathrm{V}(\mathbf{R})]|n\rangle - \sum_c \zeta_c\langle\Psi_c|n\rangle\Psi_c\right\}, \tag{16}$$

where $\zeta_n = \mathbf{g}_n^2/4\pi k$ is the eigenvalue of the plane-wave state $|n\rangle$ and the potential-function notation $\mathrm{V}(\mathbf{R})$ is

$$\mathrm{V}(\mathbf{R}) = (1/4\pi k)V(\mathbf{R}). \tag{17}$$

Using the exponential substitution $C_n = b_n\exp(-i\xi_n z)$ and switching to the Fourier transform of equation (16) yields the following equation written in the matrix form:

$$i\mathbf{M}\boldsymbol{\Gamma}\partial/\partial z\boldsymbol{\beta} = \mathbf{V}_P\boldsymbol{\Gamma}\boldsymbol{\beta}. \tag{18}$$

The matrices $\mathbf{M}$, $\mathbf{V}_P$, $\boldsymbol{\Gamma}$ and vector $\boldsymbol{\beta}$ stand for

$$\mathbf{M} = \boldsymbol{\delta} - \mathbf{G}, \tag{19}$$

where

$$(\boldsymbol{\delta})_{nk} = \delta_{nk}, \quad (\mathbf{G})_{nk} \equiv G_{nk} = \sum_c \langle\Psi_c|k\rangle\langle n|\Psi_c\rangle. \tag{20}$$

Note that the matrix $\mathbf{M}^{-1}$ can be expanded as

$$\mathbf{M}^{-1} = \boldsymbol{\delta} + \mathbf{G} + \mathbf{G}^2 + \mathbf{G}^3 + \ldots, \tag{21}$$

for which the off-diagonal elements are small compared to those on the diagonal. The non-local 'pseudo-potential' matrix $\mathbf{V}_P$ due to the screened potential takes the form

$$\mathbf{V}_P = \mathbf{V} - \mathbf{V}_c, \quad (\mathbf{V})_{nk} \equiv \langle n|V|k\rangle, \tag{22}$$

where the repulsive potential $\mathbf{V}_c$ canceling part of the attractive crystal potential $\mathbf{V}$ is

$$\mathbf{V}_c = \sum_c(\zeta_c - \zeta_k)\langle\Psi_c|k\rangle\langle n|\Psi_c\rangle. \tag{23}$$

The diagonal matrix $\boldsymbol{\Gamma}$ and column vector $\boldsymbol{\beta}$ are given by

$$(\boldsymbol{\Gamma})_{nk} = \delta_{nk}\exp(-i\xi_n z), \quad (\boldsymbol{\beta})_n = b_n. \tag{24}$$

The solution of the matrix equation (18) takes the form

$$\boldsymbol{\beta}(z) = \mathbf{S}(z, 0)\boldsymbol{\beta}(0), \tag{25}$$

where we have introduced the scattering matrix

$$\mathbf{S}(z, 0) = \delta - i\int_0^z \mathrm{d}t\,\mathbf{M}^{-1}\boldsymbol{\Gamma}^{-1}(t)\mathbf{V}_P\boldsymbol{\Gamma}(t) - \int_0^z \mathrm{d}t\,\mathbf{M}^{-1}\boldsymbol{\Gamma}^{-1}(t)\mathbf{V}_P\boldsymbol{\Gamma}(t) \times \int_0^t \mathrm{d}u\,\mathbf{M}^{-1}\boldsymbol{\Gamma}^{-1}(u)\mathbf{V}_P\boldsymbol{\Gamma}(u). \tag{26}$$

The boundary condition for the electron wavefunction $\Psi(\mathbf{R}, z)$ at the entrance surface $z = 0$ dictates that the vector $\boldsymbol{\beta}(0)$ contains only a single non-zero component $[\boldsymbol{\beta}(0)]_n = \delta_{n1}$. The complete solution can then be written as

$$\Psi(\mathbf{R}, z) = 1 + \sum_c\langle\Psi_c|0\rangle\Psi_c(\mathbf{x})[\exp(-i\zeta_c z) - 1] + \sum_n \varphi_n(\mathbf{R})\exp(-i\xi_n z)[\mathbf{S}(z, 0)_{n1} - \delta_{n1}]. \tag{27}$$

The important point is that to first order the scattering matrix scales as the pseudopotential. Since the pseudopotential is much smaller than the real crystal potential, to first order the last term in (27) can be neglected. Hence, for a reasonably thin crystal, we only need to consider the first few Wannier-(Bloch-) wave states. Note that for a thicker crystal or away from a zone-axis orientation this need not be the case and it is necessary to include extra terms *via* either a scattering-series expansion or diagonalization to yield the higher-order orthogonalized Bloch waves.

This work was supported by the Science and Technology Center for Superconductivity on NSF grant No. DMR 91-20000 and seed funding from the Center for Catalysis and Surface Science at Northwestern University.

References

Berry, M. V. & Mount, K. E. (1972). *Rep. Prog. Phys.* **35**, 315–322.
Buseck, P. R., Cowley, J. M. & Eyring, L. (1988). Editors. *High-Resolution Transmission Electron Microscopy and Associated Techniques.* Oxford University Press.
Chukhovskii, F. N., Hu, J. J. & Marks, L. D. (2000). *Acta Cryst.* A. Submitted.

Cochayne, D. J. H. & Gronsky, R. (1981). *Philos. Mag.* **44**, 159–175.
Collazo-Davila, C., Grozea, D. & Marks, L. D. (1998). *Phys. Rev. Lett.* **80**, 1678–1681.
Dorset, D. L. (1995). *Structural Electron Crystallography*. New York/London: Plenum Press.
Dorset, D. L. (1996). *Acta Cryst.* B**52**, 753–769.
Dorset, D. L. (1998). *Acta Cryst.* A**54**, 750–757.
Dorset, D. L. & Gilmore, C. J. (2000). *Acta Cryst.* A**56**, 62–67.
Dorset, D. L., Tivol, W. F. & Turner, J. N. (1992). *Ultramicroscopy*, **38**, 41–45.
Gjønnes, J., Hansen, V., Berg, B. S., Runde, P., Cheng, Y. F., Gjønnes, K., Dorset D. L. & Gilmore, C. J. (1998). *Acta Cryst.* A**54**, 306–319.
Haider, M., Rose, H., Uhlemann, S., Schwan, E., Kabius, B. & Urban, K. (1998). *Ultramicroscopy*, **75**, 53–60.
Haider, M., Uhlemann, S., Schwan, E., Rose, H., Kabius, B. & Urban, K. (1998). *Nature (London)*, **392**, 768–769.
Hauptman, H. (1982). *Acta Cryst.* A**38**, 632–641.
He, W. Z., Li, F. H., Chen, H., Kawasaki, K. & Oikawa, T. (1997). *Ultramicroscopy*, **70**, 1–11.
Hu, J. J. & Tanaka, N. (1999). *Ultramicroscopy*, **80**, 1–5.
Jayaram, G., Xu, P. & Marks, L. D. (1993). *Phys. Rev. Lett.* **71**, 3489–3492.
Kambe, K., Lempfuhl, G. & Fujimoto, F. (1974). *Z. Naturforsch. Teil A*, **29**, 1034–1041.
Kittel, C. (1963). *Quantum Theory of Solids.* New York/London: Wiley.
Marks, L. D. (1988). *Ultramicroscopy*, **25**, 85–88.
Marks, L. D. & Plass, R. (1995). *Phys. Rev. Lett.* **75**, 2172–2175.
Nicolopoulos, S., Gonzales-Calbet, J. M., Vallet-Regi, M., Corma, A., Corell, C., Guil, J. M. & Perez-Pariente, J. (1998). *Acta Cryst.* A**54**, 306–319.
Saxton, W. O. & Smith, D. J. (1985). *Ultramicroscopy*, **18**, 39–48.
Self, P. G., Glaisher, R. W. & Spargo, A. E. C. (1985). *Ultramicroscopy*, **18**, 49–62.
Sinkler, W., Bengu, E. & Marks, L. D. (1998). *Acta Cryst.* A**54**, 591–605.
Sinkler, W. & Marks, L. D. (1999*a*). *J. Microsc.* **194**, 112–123.
Sinkler, W. & Marks, L. D. (1999*b*). *Ultramicroscopy*, **75**, 251–268.
Spence, J. C. H. (1988). *Experimental High-Resolution Electron Microscopy*. Oxford University Press.
Treacey, M. M. J., Gibson, J. M. & Howie, A. (1985). *Philos. Mag.* **51**, 389–417.
Uyeda, N., Kobayashi, T., Ishizuka, K. & Fujiyoshi, Y. (1978–1979). *Chem. Scr.* **14**, 47–61.
Vainshtein, B. K. (1964). *Structure Analysis by Electron Diffraction.* Oxford: Pergamon Press.
Vainshtein, B. K., Zvyagin, B. B. & Avilov, A. S. (1992). *Electron Diffraction Techniques*, Vol. 2, edited by J. M. Cowley, pp. 216–312. Oxford University Press.
Van Dyck, D. & Chen, J. H. (1999). *Solid State Commun.* **109**, 501–505.
Van Dyck, D. & Op de Beeck, M. (1996). *Ultramicroscopy*, **64**, 99–107.
Vaughey, J. T., Thiel, J. P., Hasty, E. F., Grönke, D. A., Stern, C. L., Pöppelmeier, K. R., Dabrowski, B., Hinks, D. G. & Mitchell, A. W. (1991). *Chem. Mater.* **3**, 935–940.
Weirich, Th. E., Zou, X., Ramlau, R., Simon, A., Cascarano, G. L., Giacovazzo, C. & Hövmoller, S. (2000). *Acta Cryst.* A**56**, 29–35.
Xu, P., Jayaram, G. & Marks, L. D. (1994). *Ultramicroscopy*, **53**, 15–18.
Zandbergen, H. W., Andersen, S. J. & Jansen, J. (1997). *Science*, **277**, 1221–1225.
Zhang, H., Wang, Y. Y., Zhang, H., Dravid, V. P., Marks, L. D., Han, P. D., Payne, D. A., Radaelli, P. G. & Jorgensen, J. D. (1994). *Nature (London)*, **370**, 352–354.